Tuning the magnetic properties of the CrMnFeCoNi Cantor alloy

Timothy A. Elmslie,[1] Jacob Startt [●],[2] Yang Yang,[3] Sujeily Soto-Medina,[3] Emma Zappala [●],[4] Mark W. Meisel [●],[1,5]
Michele V. Manuel,[3] Benjamin A. Frandsen [●],[4] Rémi Dingreville [●],[2] and James J. Hamlin [●][1]

[1]*Department of Physics, University of Florida, Gainesville, Florida 32611-8440, USA*
[2]*Center for Integrated Nanotechnologies, Sandia National Laboratories, Albuquerque, New Mexico 87185, USA*
[3]*Department of Materials Science and Engineering, University of Florida, Gainesville, Florida 32611-6400, USA*
[4]*Department of Physics and Astronomy, Brigham Young University, Provo, Utah 84602, USA*
[5]*National High Magnetic Field Laboratory, University of Florida, Gainesville, Florida 32611-8440, USA*

Magnetic properties of more than 20 Cantor alloy samples of varying composition were investigated over a temperature range of 5 K to 300 K and in fields of up to 70 kOe using magnetometry and muon spin relaxation. Two transitions are identified: a spin-glass-like transition that appears between 55 K and 190 K, depending on composition, and a ferrimagnetic transition that occurs at approximately 43 K in multiple samples with widely varying compositions. The magnetic signatures at 43 K are remarkably insensitive to chemical composition. A modified Curie-Weiss model was used to fit the susceptibility data and to extract the net effective magnetic moment for each sample. The resulting values for the net effective moment were either diminished with increasing Cr or Mn concentrations or enhanced with decreasing Fe, Co, or Ni concentrations. Beyond a sufficiently large effective moment, the magnetic ground state transitions from ferrimagnetism to ferromagnetism. The effective magnetic moments, together with the corresponding compositions, are used in a global linear regression analysis to extract element-specific effective magnetic moments, which are compared to the values obtained by *ab initio* based density functional theory calculations. These moments provide the information necessary to controllably tune the magnetic properties of Cantor alloy variants.

I. INTRODUCTION

Work on high-entropy alloys began in the early 2000s with Cantor *et al.* [1]. However, the name "Cantor alloy" did not come about until a 2004 study by Yeh *et al.* [2] coined the term. Since that time, high-entropy alloys have garnered increasing attention for opening a massive number of yet-unexplored alloy systems for investigation. Already, studies have found a number of high-entropy alloys with interesting and potentially useful properties such as high hardness and resistance to anneal softening [2], shape memory effects [3,4], and superconductivity [5].

Much work has been done regarding the mechanical properties of Cantor alloys [6–11], as well as the magnetic properties of similar compounds [12–23], and previous studies on the equiatomic Cantor alloy specifically have revealed the presence of two magnetic transitions. The higher temperature transition occurs at approximately 85 K, and has been identified as spin-glass-like through μSR studies [24]. At approximately 43 K, the material transitions again, this time into a ferrimagnetic state, as determined by density functional theory (DFT) simulations and experimental analysis of the magnetic entropy [24]. Despite the small size of the ferrimagnetic transition, prior work has suggested that it is not due to an impurity phase [24]. Other studies have observed notable differences in the size and temperature of these transitions, likely due to the significant processing dependence of the Cantor alloy [25–27]. Not only are the magnetic properties of the alloy highly sensitive to annealing

and cold-working [28–30], high-temperature anneals do not eliminate the effects of cold-working. This phenomenon may be related to recent discoveries by Miyajima *et al.* [31] and Wang *et al.* [32]. Miyajima *et al.* observed that cold-working gradually broke down and ultimately destroyed mesoscopic domains within an induction-melted Cantor alloy sample, while Wang *et al.* reported the same phenomenon in a number of Cantor alloy samples of varying composition which were prepared via arc melting followed by homogenization at 1200 °C and water quenching. Analysis which combined modified Curie-Weiss fitting, specific heat measurements, DFT calculations and Hall measurements has also revealed a large Stoner enhancement factor [24]. Certain studies have also experimented with adjusting the properties of high-entropy alloys, such as a 2021 paper by Na *et al.* [33], which examined the hard magnetic properties of high entropy alloys consisting of Fe, Co, Ni, Al, Cu, and Ti in a variety of different compositions. In the Cantor alloy specifically, Lee *et al.* [34] found that the overall magnetization of the compound was increased as the Mn content was reduced, until a ferromagnetic transition was revealed at 0% Mn, and Wagner *et al.* varied the Cr/Ni ratio in the Cantor alloy, finding that the ratio had little effect on lattice constants. However, they did observe that as the Cr/Ni ratio grew the solidus temperature increased while the staking fault energy fell.

Additionally, few papers have reported the magnetic properties of four-element combinations of the Cantor alloy, but the nature of the magnetic states has not been universally established. For example, Kao *et al.* [14], Lucas *et al.* [15],

and Tan *et al.* [35] all investigated CrFeCoNi, but Lucas *et al.* stated that the compound is paramagnetic at low temperature, while Kao *et al.* and Tan *et al.* claim that it is ferromagnetic. Tan *et al.* also observed significant differences between the lattice distortion of CrFeCoNi as a function of temperature compared to nonferromagnetic formulations of the Cantor alloy, suggesting that the lattice distortion and magnetic properties are closely related. In this paper, a number of four-element compounds were synthesized and measured alongside numerous five-element compounds with varying compositions in order to resolve these issues. Wagner *et al.* [36] recently examined the effects of varying the composition of the Cantor alloy by adjusting the amount of Cr and Ni relative to one another. Though their work largely focused on physical properties such as lattice constants, elastic moduli, and stacking fault energy, they also observed ferromagnetism at approximately 200 K and above in samples with relatively large concentrations of Ni and low concentrations of Cr.

Computational works have also begun to address accurately modeling the properties of the Cantor and related medium and high-entropy alloys, such as Woodgate and Staunton [37], who developed a fast *ab initio* method of determining Gibbs free energy, and therefore phase stability of high- and medium-entropy alloys, using the Cantor alloy and certain variants as a case study. Similarly, Moitzi *et al.* [38] developed an *ab initio* technique to model solid solution strengthening in high- and medium-entropy alloys which predicted the properties of the Cantor alloy and certain variants thereof with good accuracy.

Our measurements of magnetic susceptibility on more than 20 Cantor alloy samples with varying compositions reveal that increasing the relative amount of ferromagnetic elements, such as Fe, enhances the overall magnetization, while larger quantities of antiferromagnetic elements decrease the magnetization. This observation is consistent with previous Cantor alloy investigations, which reported Fe, Co, and Ni tend to align ferromagnetically while Cr and Mn are typically antiferromagnetic [23,24,26]. Herein, these trends are quantified by least-squares analysis performed using effective moments of each of the measured samples, revealing that element-specific magnetic moments can be estimated for samples that are close to the equiatomic composition. However, the magnetic properties change when the effective moment becomes sufficiently large due to a lack of antiferromagnetic elements or a relative abundance of ferromagnetic ones. At this point, the compound becomes ferromagnetic rather than ferrimagnetic at low temperature, as evidenced by muon spin-relaxation studies on select samples in the Mn series. Our experimental results, combined with *ab-initio*-based DFT calculations, provide a complete picture of the compositional dependence of the magnetic properties of the Cantor alloy system. This paper highlights the great promise of similar regression analysis methods applied to several chemically substituted alloy samples to provide insights into elemental specific contributions to properties in other high-entropy materials.

II. METHODS

This section describes the details of the various experimental and computational methods that were employed in this paper, including the sample synthesis, magnetic and structural characterization, and DFT calculations.

A. Synthesis

Samples were synthesized by combining stoichiometric quantities of elemental Cr, Mn, Fe, Co, and Ni in an Edmund Bühler MAM-1 Compact Arc Melter. Chromium, manganese, iron, and nickel were sourced from Alfa Aesar, while cobalt was purchased from Cerac. The chromium used for synthesis was 99.995% pure, while the cobalt was 99.5% pure. All other elements were 99.95% pure. Each sample was melted five times, flipping it over between each melt to improve sample homogeneity. Following synthesis, samples were sealed in quartz tubes in Ar atmosphere and annealed at 1100 °C for six days, then quenched in water before measurement. However, the samples consisting of 25% of one element and 18.75% of every other element (25% samples) were annealed first for six days at 1080 °C and then again at 1100 °C, quenching in water following each anneal. The additional anneal was related to an issue with the furnace thermocouples. When the initial annealing was determined to be lower than the 1100 °C target, the samples were reannealed at this temperature as described.

B. Sample nomenclature

To simplify the process of investigating varying compositions, in each sample, the amount of only one element was adjusted, and all other elements remained in an equiatomic ratio according to the atomic ratios, $A_x[BCDE]_{100-x}$. For example, when adjusting the amount of Mn, sample compositions would follow the pattern $Mn_x(CrFeCoNi)_{100-x}$. This practice permits a simplified notation, listing only the element with an adjusted quantity and the percentage of that element present in the alloy. From that information alone, the relative proportion of other elements can then be inferred. For example, Cr_{22} is used instead of writing $Cr_{22}(MnFeCoNi)_{78}$, and a sample with composition CrFeCoNi is represented by the abbreviation Mn_0. This convention is used from this point onward in this work. Samples with an equal proportion of each element (equiatomic) are listed as Equi.

C. Magnetic characterizations

Magnetization and susceptibility measurements were performed using a Quantum Design Magnetic Property Measurement System. Small pieces ranging from a few milligrams to a few hundred milligrams (typically ≈ 50 mg), were cut from larger samples using an Allied 3000 low speed saw to minimize unintentional working of the samples. Each sample was secured in a gel capsule inside a plastic straw for measurement.

Muon spin spectroscopy measurements (μSR) were conducted at TRIUMF Laboratory in Vancouver, Canada using the LAMPF spectrometer on the M20D beamline. The μSR technique utilizes the asymmetric decay of initially spin-polarized positive muons into positrons to probe the magnetic properties of the sample [39]. Specifically, μSR is uniquely sensitive to the volume fraction of different magnetic and nonmagnetic phases, which is important for potentially inhomogeneous systems such as magnetic alloys.

The experimentally measured quantity is the time-dependent asymmetry, $a(t)$, which is determined from the difference in positron events between two detectors placed on opposite sides of the sample. The asymmetry is proportional to the component of the net muon spin polarization along the axis connecting the two detectors. Information about the local magnetic field distribution can be inferred from the behavior of $a(t)$ as a function of temperature and applied magnetic field. Additional details about our experimental configuration are described elsewhere [24], and the open source program BEAMS [40] was used for data analysis.

D. Structural and composition characterizations

The crystal structure of the sample was investigated using a Panalytical Xpert X-Ray Diffraction (XRD) with a Cu K-alpha radiation source at a voltage of 45 kV and current of 40 mA in the 2θ range of $30 - 100°$. The powder samples were prepared using a steel file. The microstructure of the sample was characterized using a Tescan MIR3 scanning electron microscope (SEM) at 20 kV. The expoxy-mounted sample was first ground using a series of SiC paper at steps of 600 grit, 800 grit, and 1200 grit, then further polished using alcohol-based lubricant and diamond paste in the sequence of 6 μm, 3 μm, and 1 μm. The sample surface was polished using 0.05 μm water-free colloidal silica suspension. The chemical composition of the sample was determined using an equipped energy-dispersive x-ray detector. Additional details of composition and possible impurity phases are presented in the Supplemental Material [41] (see also Refs. [42,43] therein).

E. Computational methods

Ab-initio-based DFT calculations were performed in parallel to experimental investigations to study the net moment behavior of the low-temperature ferrimagnetic phase as a function of composition. All DFT calculations were performed in the spin-collinear polarized state using the VIENNA AB-INITIO SIMULATION PACKAGE [44–46]. Electronic wave functions were thus modeled using plane waves while the interaction between the frozen core states and valence states was handled according to the projector-augmented wave formalism [47,48]. Exchange and correlation was treated according to the generalized gradient approximation as parameterized by Perdew *et al.* [49].

The modeled Cantor compositions were selected according to the same convention used in the experimental analysis, such that only one element was varied at time, according to $A_x[BCDE]_{100-x}$, resulting in five separate series of simulations (i.e., one for each species). Within each series, four compositions were modeled (i.e., $x = 10, 20, 30, 40$). The alloys were modeled using supercells containing 108 atoms, constructed as $3 \times 3 \times 3$ cubic multiplications of the conventional four-atom FCC unit cell. Three separate supercells, each with a randomized ordering of the atoms among the lattice sites, were constructed for each composition modeled. Thus, any reported properties represent the average of the three random solution supercells at each composition.

For all calculations, a $5 \times 5 \times 5$ gamma-centered k-point mesh, along with a plane-wave energy cutoff of 400 eV and a Gaussian smearing smearing width of 0.01 eV was found to sufficiently minimize fluctuations in the total energy and magnetic moments. The minimization threshold of the total energy with respect to the electronic convergence was set to 1.0×10^{-6} eV, while the ionic convergence threshold was met when forces on all atoms fell below 20×10^{-3} eV Å^{-1}.

III. RESULTS

In this section, the results of magnetization as a function of temperature and magnetic field are described along with the low-temperature μSR data. These experimental findings are analyzed and contrasted with the DFT work in the next section.

A. Magnetization

In Fig. 1, results of susceptibility versus temperature measurements are presented on the left side, while magnetization versus field results are shown on the right. Each row displays a collection of samples, grouped according to the elemental concentration being adjusted. Due to their strong magnetic response, most of the $x = 0$ samples are not included in this figure, with Fe$_0$ as an exception, so the composition dependence of the trends and features of the $x > 0$ data can be more easily compared. The Cr$_0$ and Mn$_0$ data sets are plotted in Fig. 2.

Three striking features are identified in the plots shown in Fig. 1. First, a spin-glass-like transition (T_2), marked by a peak [24,26], occurs at high temperatures, which varies widely depending on composition. For example, this feature is apparent in the Fe$_{30}$ data set at about 67 K, and its presence in the other Fe samples varies within a few degrees [Fig. 1(e)]. The spin-glass-like peak, if present, has a stronger composition dependence for the Cr, Mn, Co, and Ni samples, where variations of tens of kelvin are present [Figs. 1(a), 1(c), 1(g), and 1(i)]. Second, a steplike feature (T_1) appears in many data sets, marking a ferrimagnetic transition [24], as clearly present in the Mn$_{25}$ susceptibility data, Fig. 1(c). In all samples in which it appears, the T_1 feature occurs at 43(1) K, and although this robustness might be considered a fingerprint of an impurity phase, prior work has established this transition to be intrinsic to the Cantor alloy [24]. Lastly, another feature (T^*) occurs in several samples at approximately 18 K and is most obvious in the Mn$_{25}$ data, Fig. 1(c). The nature of the T^* feature is unclear, but may be the result of differences in processing. The $x = 25$ samples were annealed and quenched twice, once at 1080 K and then at 1100 K, whereas other samples in which T^* appears were annealed and subsequently quenched in the same quartz tube along with several more pieces (up to as many as five), which may have resulted in a slower quench.

The magnetization versus field data along the right side of Fig. 1 shows that even at fields of up to 70 kOe, magnetization remains a small fraction of a Bohr magneton. For example, the Fe$_{25}$ sample reaches approximately 0.03 μ$_B$ atom^{-1}, much smaller than the Hund's-rule-predicted effective moments for the constituent elements, which is typically a few μ$_B$ atom^{-1} [50]. Thus, near-equiatomic compositions of the Cantor alloy are far from magnetic saturation saturation even at 70 kOe. Even in Mn$_{10}$, which extends beyond the limits of the y axis
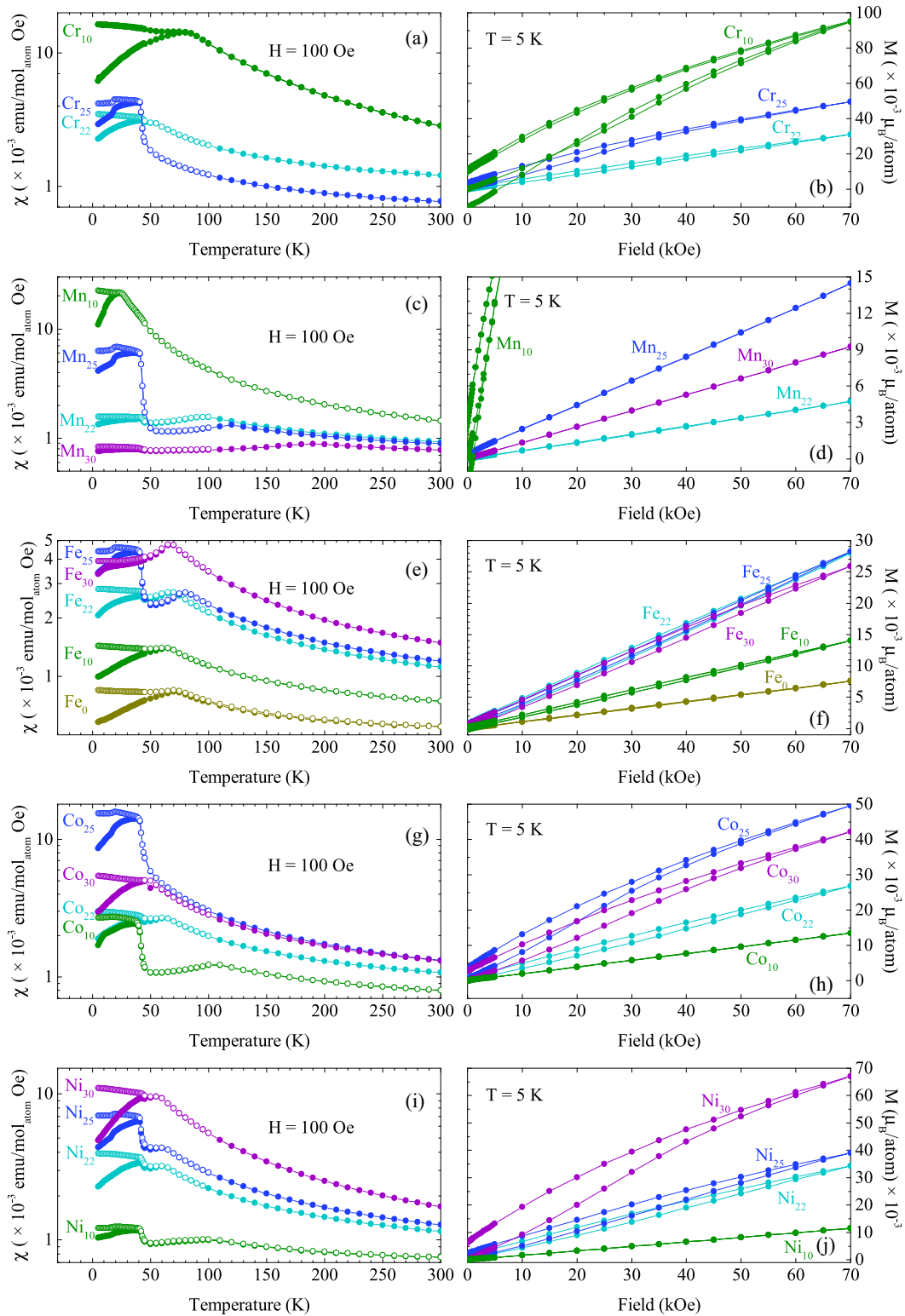
FIG. 1. Susceptibility and magnetization data for Cantor alloys of varying compositions. Panels on the left show susceptibility versus temperature on a logarithmic scale, while those on the right show magnetization as a function of magnetic field. In the susceptibility plots, solid circles represent zero-field cooled (ZFC) data, which were measured after cooling in zero field. Open circles represent field-cooled warming (FCW) data, which were collected after cooling in an applied field of 70 kOe. Each row displays a different set of compounds: [(a), (b)] Cr-varied compositions; [(c), (d)] Mn-varied compositions; [(e), (f)] Fe-varied compositions; [(g), (h)] Co-varied compositions, and [(i), (j)] Ni-varied compositions. Section II B describes the sample nomenclature. Certain curves such as Mn_{10} and Fe_{30} display only one feature. In these cases, the feature is identified as T_1 or T_2 depending on its shape, with T_1 being steplike and T_2 being a peak.
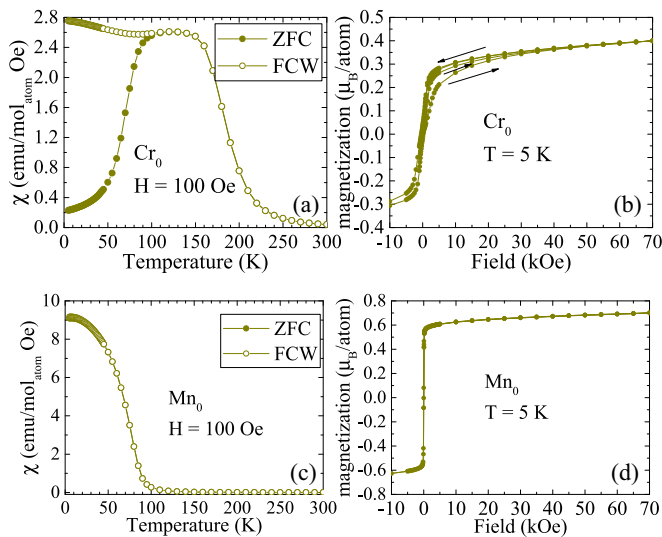
FIG. 2. Magnetic susceptibility as a function of temperature for the (a) Cr_0 and (c) Mn_0 samples. Magnetization as a function of applied field for the (b) Cr_0 and (d) Mn_0 samples. Magnetization data for Cr_0 show significant hysteresis, and arrows in (b) indicate the direction of the magnetic field sweep for each curve segment. In (c), ZFC and FCW curves are difficult to distinguish due to significant overlap, with less than 1% of difference across the entire data range.

[Fig. 1(d)], the magnetization reaches only $0.08\,\mu_B\,\text{atom}^{-1}$ at 70 kOe. One trend visible in Fig. 1 is that hysteresis increases

as susceptibility increases, perhaps indicating the presence of ferromagnetic regions within the material.

The plots of Fig. 1 also reveal that susceptibility increases with greater proportions of ferromagnetic elements Fe, Co, or Ni. On the other hand, increasing the relative amount of antiferromagnetic elements Cr or Mn decreases the susceptibility. At sufficiently low concentrations of Cr or Mn, the magnetic properties change significantly, resulting in larger saturation magnetization and susceptibility. Consequently, Cr_0 and Mn_0 data are excluded from Fig. 1 and are instead presented in Fig. 2. The Cr_0 sample reaches susceptibility values of approximately $9.1\,\text{emu mol}_{atom}^{-1}\text{Oe}^{-1}$, much larger than the susceptibility maximum of, for example, Mn_{25} of about $6.8 \times 10^{-3}\,\text{emu mol}_{atom}^{-1}\text{Oe}^{-1}$. Although the susceptibility and saturation magnetization of the Cr_0 and Mn_0 samples are orders of magnitude larger than those shown in Fig. 1, they are still lower than effective moments predicted by Hund's rule [50]. These Cr_0 and Mn_0 samples also possess a single ferromagnetic transition compared to the ferrimagnetic and spin-glass-like transition of the near-equiatomic samples. These behaviors are consistent with data previously published by Wagner *et al.* [36], who observed ferromagnetism in Cantor alloy samples containing less than 5 at. % Cr and more than 35 at. % Ni, and Lee *et al.* [34], who also observed a ferromagnetic transition in Mn_0. The Mn_{10}, which exhibits a somewhat enhanced susceptibility that makes it clear this sample is close to a transition to ferromagnetism that occurs somewhere between Mn_{10} and Mn_0.

TABLE I. Transition temperatures and modified Curie-Weiss fitting parameters of each measured alloy.

Composition	T_1 (K)	T_2 (K)	$\chi_0(\times 10^{-3}\text{emu mol}_{atom}^{-1}\text{Oe}^{-1})$	p_{eff} (μ_B)	θ (K)
Equi [a]	44	82	5.57(4)	0.98(10)	−8.9(8)
Cr_0 [b,c]	180				
Cr_{10} [b]	44	80	−10.1(5)	2.9(4)	15.6(9)
Cr_{22}	44	55	7.761(16)	1.02(6)	−5.10(21)
Cr_{25}	42		5.287(22)	0.77(7)	−9.6(5)
Mn_0 [b,c]	75 [d]				
Mn_{10}	44		1.75(23)	1.67(19)	13.3(5)
Mn_{22}	43	100	5.640(27)	0.95(9)	−11.6(9)
Mn_{25}	42	120	5.608(28)	0.91(10)	−16.8(1.2)
Mn_{30}	43	190 [d]	6.07(27)	0.6(3)	14(29)
Fe_0		70	4.667(23)	0.44(7)	9.5(1.5)
Fe_{10}		65	5.281(20)	0.73(7)	−11.7(8)
Fe_{22}	43	67	5.868(9)	1.13(5)	−5.20(14)
Fe_{25}	42	80	5.80(3)	1.23(10)	−7.2(5)
Fe_{30}		67	5.09(14)	1.51(18)	2.9(1.0)
Co_{10}	42	105	5.264(16)	0.83(7)	−13.6(7)
Co_{22}	43	62	6.079(13)	1.07(6)	−4.37(19)
Co_{25}	42		4.93(5)	1.39(10)	3.4(3)
Co_{30}		50	5.60(3)	1.34(8)	0.15(21)
Ni_{10}	43	100	6.35(3)	0.53(10)	9.2(2.9)
Ni_{22}	43	60	5.653(17)	1.18(6)	−4.20(19)
Ni_{25}	42	60	4.44(3)	1.40(9)	−1.27(24)
Ni_{30}	44	55	0.05(17)	1.96(19)	10.0(6)

[a]Data on the equiatomic compound were obtained by averaging values from four samples.
[b]Mark samples that could not be accurately fit by the modified Curie-Weiss equation or produced unphysical results from fitting.
[c]Indicate samples which become ferromagnetic below the T_1 transition temperature, as opposed to the ferrimagnetic state assumed by other samples.
[d]Indicate transition temperatures that were confirmed via muon spin-relaxation measurements.
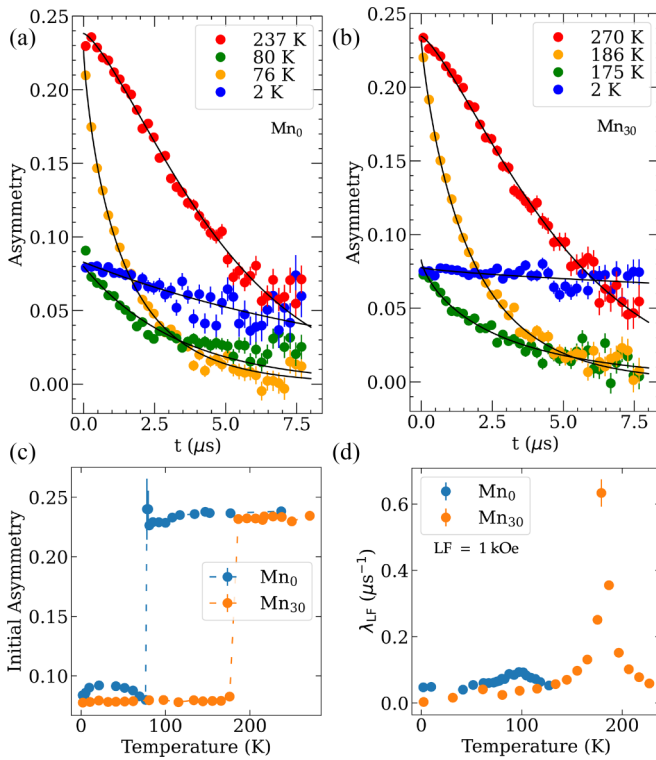
FIG. 3. [(a), (b)] Representative zero-field μSR asymmetry spectra for Mn$_0$ and Mn$_{30}$, respectively. (c) Temperature dependence of the initial asymmetry at $t = 0$ for both samples, showing a sharp step at the expected transition temperatures. (d) Temperature dependence of the long-time relaxation rate λ_{LF} in an applied longitudinal field of 1 kOe.

Transition temperatures for each measured sample are summarized in Table I. The positions of the lower temperature (steplike) transitions were determined by local minima of the first derivative, while the critical temperature of the higher temperature transitions are located at the peak in the magnetic susceptibility. In several of the iron samples, the ferrimagnetic transition is either absent or too small to detect, and the spin-glass/antiferromagnetic transition is not visible in the ferromagnetic (Cr$_0$ and Mn$_0$) or nearly ferromagnetic (Mn$_{10}$) samples.

B. Muon spin spectroscopy

μSR measurements of Mn$_0$ and Mn$_{30}$ alloys were conducted to evaluate the magnetic homogeneity and confirm the magnetization results. Representative $a(t)$ asymmetry spectra collected in zero applied magnetic field (ZF) are shown in Figs. 3(a) and 3(b) for Mn$_0$ and Mn$_{30}$, respectively. For both samples, the gentle relaxation of the asymmetry at high temperature becomes more rapid as the temperature is lowered toward the transition due to critical slowing down of spin fluctuations. Between $77 - 80$ K for Mn$_0$ and $175 - 185$ K for Mn$_{30}$, the initial asymmetry value at $t = 0$ drops to approximately 1/3 of its high-temperature value, signifying the onset of static magnetism [39]. These temperatures agree well with $T_1 = 75$ K for Mn$_0$ and $T_2 = 190$ K for Mn$_{30}$ given in Table I. The narrow temperature range in which the initial

asymmetry drops demonstrates that the magnetic transition is sharp and uniform throughout the entire volume of the sample, *confirming that the nonstoichiometric alloys are similarly magnetically homogeneous as the equiatomic alloy* [24]. The uniform magnetic behavior of each sample is further illustrated in Fig. 3(c), where the initial asymmetry plotted as a function of temperature shows an abrupt step at the transition. The initial asymmetry was determined by fitting the generalized exponential function $a(t) = a_0 \exp(-\lambda t)^\beta$ to the spectra, as was done previously [24]. It is noteworthy that a characteristic Kubo-Toyabe relaxation pattern [51] is observed for Mn$_0$ within the first ~100 ns of the spectra below the transition, but is not visible on the timescale used in Fig. 3(a), in contrast to Mn$_{30}$ and the equiatomic alloy [24], indicative of subtle composition-dependent changes of the internal magnetic field distribution at the muon stopping sites.

Finally, Fig. 3(d) displays the temperature-dependent relaxation rate λ_{LF} of the long-time asymmetry for data collected in an applied longitudinal field (LF) of 1 kOe (not shown), which is a sensitive probe of spin dynamics. The values of λ_{LF} were determined from generalized exponential fits to the LF asymmetry spectra. Mn$_0$ shows a low, broad peak in λ_{LF} centered around 90 K (slightly above the transition temperature in ZF), while Mn$_{30}$ shows a much higher and sharper peak centered around 180 K. These results point to differences in the spin dynamics of the two samples, with critical behavior being suppressed in Mn$_0$ and preserved in Mn$_{30}$. A more detailed theoretical investigation of the microscopic magnetic behavior of Cantor alloys with various Mn compositions could help explain these differences in the ZF and LF data of the Mn$_0$ and Mn$_{30}$ samples.

IV. DISCUSSION

A. Modified Curie-Weiss fitting

Previous work [24] on fitting magnetic susceptibility data for the equiatomic Cantor alloy has revealed the need for a modified Curie-Weiss equation

$$\chi(T) = \chi_\mathrm{o} + \frac{C_m}{T - \theta}, \tag{1}$$

in which C_m is the Curie constant, θ is the Curie-Weiss temperature, and χ_o is a constant that represents the summation of multiple temperature-independent terms such as Pauli paramagnetism, Van Vleck paramagnetism, Landau diamagnetism, and core diamagnetism [52–56]. One can obtain an effective moment p_{eff} from this fitting using [57]

$$p_{\mathrm{eff}} = 2.82 \, C_m^{1/2}. \tag{2}$$

In the Cantor alloy, Stoner-enhanced Pauli paramagnetism dominates the χ_o term, and diamagnetic contributions were predicted to be, at most, 5% of the size of the enhanced Pauli paramagnetism [24]. Van Vleck paramagnetism is present in compounds with a total angular momentum $J = 0$ ground state. In the Cantor alloy, this state may occur in Cr^{2+} and Mn^{3+}, though further work is required to determine whether this mechanism plays a significant role.

Fitting Eq. (1) to the field-cooled susceptibility data produces best fit values of χ_0, p_{eff}, and θ for 23 different samples. In each case, the data were fit from 300 K down to

temperatures just above the highest temperature magnetic ordering transition. The parameters derived from fitting each measured sample are summarized in Table I. Figure S2 (Supplemental Material [41]) compares the susceptibility with the fit to Eq. (1) for each sample, demonstrating excellent agreement in almost all cases. Fit parameters are not reported for the two samples that appear to have transitioned to a distinct ferromagnetic ground state, Mn_0 and Cr_0. For these two samples the fit was unreliable, producing values that were unphysical or depended significantly on the temperature range of the fit.

Several conclusions are immediately apparent on review of Table I. While the values of the Curie-Weiss temperature, θ, remain close to zero, systematic trends are absent. The temperature-independent susceptibility, χ_0, is consistently of order $\sim 5 \times 10^{-3}$ emu $mol_{atom}^{-1}Oe^{-1}$. However, systematic trends in χ_0 are also largely absent, except perhaps in the case of the Ni series. On the other hand, the effective moments, p_{eff} show very clear trends across each substitutional series. These trends are illustrated in Fig. 4(a), where it is immediately clear that Cr and Mn suppress the susceptibility, while Fe, Co, and Ni have the opposite effect.

B. Element-specific average magnetic moments

Average element-specific magnetic moments can be estimated via a least-squares method using the effective moments in Table I. Assuming that each element contributes to the total effective moment as a linear function of its concentration, the net effective moment of the compound can be expressed as

$$p_{\text{eff}} = \sum_i C_i \, p_i \,, \tag{3}$$

in which C_i is the concentration of element i, and p_i is the effective moment of that element. For example, the net effective moment of Ni_{25} could be estimated as

$$0.25 \, p_{Ni} + 0.1875(p_{Cr} + p_{Mn} + p_{Fe} + p_{Co}) = p_{\text{eff},Ni_{25}}, \tag{4}$$

and similar equations can be generated for each of the samples for which p_{eff} values are given in Table I. If one assumes the element-specific magnetic moments are constant across all samples, an overdetermined system of equations with only five unknowns is obtained. This set of linear equations can be solved by linear regression to produce best-fit values of the five element-specific magnetic moments. Additional details of the fitting process are described in the Supplemental Material [41].

The resulting element-specific moments are tabulated in Table II. The extracted moments are of order a few μ_B, similar to typical experimental values found for these elements and also of the same order as the Hund's rules values [50]. However, the Cr and Mn moments enter as negative values, suggesting these elements exhibit a strong antiferromagnetic interaction. The solid lines in Fig. 4 are generated for each substitutional series using the moments listed in Table II together with Eq. (2). Strikingly, this single set of five element-specific moments produces excellent agreement with the experimentally determined net effective moment across a wide range of compositions.
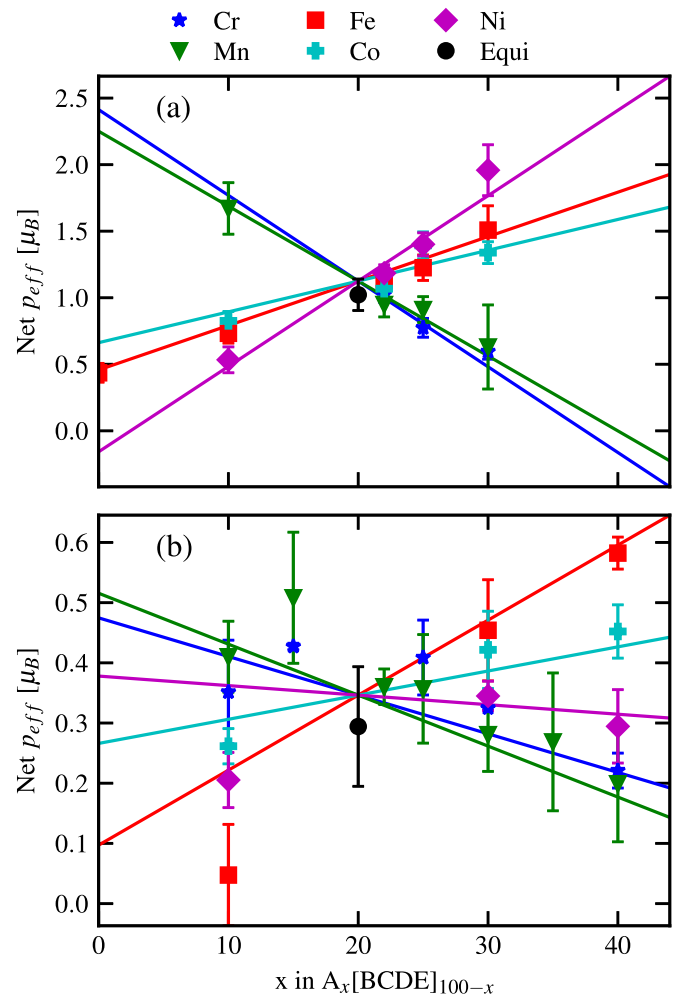

FIG. 4. Net magnetic moment versus composition for each series of samples for (a) experimental data and (b) DFT simulations. Each point corresponds to a single sample. Adding Fe, Co, or Ni tends to increase the net moment, while adding Cr or Mn suppresses the net moment. The solid lines represent a model of the data based on element-specific p_{eff} values listed at the bottom of the figure. The element-specific p_{eff} values were determined through a global linear least-squares regression of all of the available data as described in the text.

C. Comparison of DFT and experiment

Previous DFT calculations of the equiatomic Cantor alloy suggested a ferrimagnetic ordering at absolute zero [24], where the Fe, Co, and Ni species and the Cr and Mn species

TABLE II. Effective moments and their uncertainties extracted via least-squares regression compared with empirical effective moments as tabulated in Blundell [50].

Source	p_{Cr}	p_{Mn}	p_{Fe}	p_{Co}	p_{Ni}
This paper (experiment)	−5.0(1.2)	−3.1(1.2)	3.8(3)	3.2(4)	6.5(7)
This paper (DFT)	−0.2(1)	−0.3(1)	1.3(2)	0.7(1)	0.3(4)
Ionization 2+ [50]	4.82	5.82	5.36	4.90	3.12
Ionization 3+ [50]	3.85	4.82	5.82		

couple ferromagnetically and antiferromagnetically, respectively. In this paper, the compositional dependence of the net moment was modeled in parallel to the experimental study, probing the dependence on a per species basis in the same manner as the experimental investigation. These results are shown in Fig. 4(b), where the net moment, as calculated by DFT, is plotted as a function of the variation of each species in the alloy, such that $A_x[BCDE]_{100-x}$ represents the overall composition. In a similar fashion, a leasts-square fit is applied to the set of DFT calculated moments to obtain effective local moments of the individual species (see Table II). Both DFT and experimentally derived element-specific moments exhibit consistent signs, i.e., they are in agreement on the ferro- and antiferromagnetic tendency of each species. However, the magnitudes of the effective moments differ. Specifically, they differ on the ferromagnetic strengths of Fe and Ni and on the relative antiferromagnetic strength between Cr and Mn. Notably, DFT calculations predict a weak decrease in the net effective moment with increasing Ni concentration, contrary to experimental results. This discord occurs despite the positive moment produced by the linear regression analysis of the DFT moments for Ni. In fact, this behavior can be understood as being due to the rather small Ni moment compared to the moments of Co and Fe, such that increasing Ni concentration proportionally decreases Co and Fe content, which lowers the overall net moment.

There could be several reasons for the discrepancy in the element specific moments from the analysis of DFT versus experimental data. First, the experimental p_{eff} moments were fit to susceptibility data measured in the temperature range of the paramagnetic state, i.e., above any magnetic ordering transition temperature. The DFT p_{eff} moments, on the other hand, were calculated at absolute zero, squarely within the temperature range corresponding to the ferrimagnetic state. Attempting to model the compositional dependence of the paramagnetic state through DFT, however, is not computationally feasible and would likely be subject to errors common to the approximations needed to depict the paramagnetic state in DFT.

Independent of the overall magnetic state, another potential contributing factor for the discrepancy between computationally and experimentally derived moments may be related to thermal expansion. The average volume associated with each atomic lattice site is a factor that has been shown have significant influence on the local magnetic moment behavior of species in this alloy [58]. As the volume of the lattice site increases, the magnitude of the local moment of each species may also change at different rates. In the case of Mn, Ma *et al.* [58] even showed the net direction of the average Mn spin tended to flip from down to up (or from antiferromagnetic to ferromagnetic) as the atomic volume increases. While the total amount of thermal expansion in the low-temperature regime investigated here ($T < 300$ K) is likely small, effects on the local and net moment behavior may still be present.

Billington *et al.* [59] carried out a detailed study of the element-specific magnetic properties of the Cantor alloy and certain Cantor alloy variants using a combination of magnetic Compton scattering, x-ray magnetic circular dichroism spectroscopy, and bulk magnetization measurements, noting significant discrepancies between computational and experimental results when examining magnetic moments. However,

in compounds where computation and experiment disagreed, computational moments were much larger than experimental ones. For instance, they measured a net moment of 0.008 μ_B in a SQUID magnetometer for the equiatomic Cantor alloy, while different theoretical calculations predicted moments between 0.4 and 0.9 μ_B. However, one should note that the small moment reported from SQUID measurements appears to be based on a high field saturation moment, which is similar in magnitude to the typical magnetization observed at 70 KOe (see Fig. 1). Billington *et al.* attributed these discrepancies to the spin-glass behavior observed in the Cantor alloy and/or an unconventional magnetic ground state. Concerning the present paper, the fact that effective moments extracted from modified Curie-Weiss fits are large compared to the magnetization at 70 kOe (and large compared to DFT calculated moments) is fully consistent with the picture that the Cantor alloy is a Stoner-enhanced itinerant magnet [24]. Such systems can exhibit very large ratios of the effective moment to the saturation moment [60].

Finally, the moments extracted from our linear regression analysis and tabulated in the first row of Table II should not be expected to correspond exactly to element-specific moments directly determined via methods such as inelastic x-ray scattering. Rather, they give the overall incremental contribution to the net effective moment as the concentration of one component of the alloy is adjusted. As such, these moments provide a useful guide to efforts to design Cantor alloy variants with specific magnetic properties.

V. CONCLUSIONS

Near the equiatomic composition, the Cantor alloy undergoes two transitions, a ferrimagnetic transition at lower temperature and a spin-glass-like transition at higher temperature. While the spin-glass-like transition temperature varies depending on concentration, the ferrimagnetic transition is remarkably stable, occurring at approximately 43 K in all samples in which it appears despite not resulting from an impurity phase [24]. Trends in the magnetic properties are clearest in the Mn samples, in which larger concentrations shift the spin-glass-like transitions to higher temperatures and decrease the net effective moment. In alloys with low concentrations of Cr or Mn, however, the ferrimagnetic transition becomes ferromagnetic.

Fitting the susceptibility of Cantor alloy samples of many different compositions permits the estimation of the magnetic contribution from each constituent element by assuming a linear contribution from each. This analysis reveals that larger concentrations of ferromagnetic elements Fe, Co, and Ni increase the net effective magnetic moment of the Cantor alloy, while increased quantities of antiferromagnetic elements Cr and Mn decrease the net effective moment. The effective magnetic moments extracted via this process provide a road map facilitating a fine level of control over the magnetic moment of the Cantor alloy by varying its composition. Furthermore, similar regression analyses of data for a variety of chemically substituted samples could be extended to a wider range of high-entropy materials to provide similar insight into the composition dependence of a other properties.

[1] B. Cantor, K. B. Kim, and P. J. Warren, J. Metastable Nanocryst. Mater. **13**, 27 (2002).

[2] J.-W. Yeh, S.-K. Chen, S.-J. Lin, J.-Y. Gan, T.-S. Chin, T.-T. Shun, C.-H. Tsau, and S.-Y. Chang, Adv. Eng. Mater. **6**, 299 (2004).

[3] G. S. Firstov, T. A. Kosorukova, Y. N. Koval, and V. V. Odnosum, Mater. Today: Proc. **2**, S499 (2015).

[4] C.-H. Chen and Y.-J. Chen, Scr. Mater. **162**, 185 (2019).

[5] K. Motla, V. Soni, P. K. Meena, and R. P. Singh, Supercond. Sci. Technol. **35**, 074002 (2022).

[6] B. Cantor, I. T. H. Chang, P. Knight, and A. J. B. Vincent, Mater. Sci. Eng. A **375**, 213 (2004).

[7] F. Otto, A. Dlouhý, C. Somsen, H. Bei, G. Eggeler, and E. P. George, Acta Mater. **61**, 5743 (2013).

[8] M. Laurent-Brocq, A. Akhatova, L. Perrière, S. Chebini, X. Sauvage, E. Leroy, and Y. Champion, Acta Mater. **88**, 355 (2015).

[9] M. J. Jang, S. Praveen, H. J. Sung, J. W. Bae, J. Moon, and H. S. Kim, J. Alloys Compd. **730**, 242 (2018).

[10] J. H. Kim, K. R. Lim, J. W. Won, Y. S. Na, and H.-S. Kim, Mater. Sci. Eng.: A **712**, 108 (2018).

[11] S.-W. Kim and J. H. Kim, Mater. Sci. Eng.: A **718**, 321 (2018).

[12] X. Wang, Y. Zhang, F. Qiao, and G. Chen, Intermetallics **15**, 357 (2007).

[13] K. Zhang, Z. Fu, J. Zhang, J. Shi, W. Wang, H. Wang, Y. Wang, and Q. Zhang, J. Alloys Compd. **502**, 295 (2010).

[14] Y.-F. Kao, S.-K. Chen, T.-J. Chen, P.-C. Chu, J.-W. Yeh, and S.-J. Lin, J. Alloys Compd. **509**, 1607 (2011).

[15] M. S. Lucas, L. Mauger, J. A. Muñoz, Y. Xiao, A. O. Sheets, S. L. Semiatin, J. Horwath, and Z. Turgut, J. Appl. Phys. **109**, 07E307 (2011).

[16] S. Singh, N. Wanderka, K. Kiefer, S. Siemensmeyer, and J. Banhart, Ultramicroscopy **111**, 619 (2011).

[17] L. Liu, J. B. Zhu, J. C. Li, and Q. Jiang, Adv. Eng. Mater. **14**, 919 (2012).

[18] S. Ma and Y. Zhang, Mater. Sci. Eng. A **532**, 480 (2012).

[19] K. Zhang and Z. Fu, Intermetallics **28**, 34 (2012).

[20] M.-H. Tsai, Entropy **15**, 5338 (2013).

[21] Y. Zhang, T. Zuo, Y. Cheng, and P. K. Liaw, Sci. Rep. **3**, 1455 (2013).

[22] Z. Leong, J. S. Wróbel, S. L. Dudarev, R. Goodall, I. Todd, and D. Nguyen-Manh, Sci. Rep. **7**, 39803 (2017).

[23] T. Zuo, M. C. Gao, L. Ouyang, X. Yang, Y. Cheng, R. Feng, S. Chen, P. K. Liaw, J. A. Hawk, and Y. Zhang, Acta Mater. **130**, 10 (2017).

[24] T. A. Elmslie, J. Startt, S. Soto-Medina, Y. Yang, K. Feng, R. E. Baumbach, E. Zappala, G. D. Morris, B. A. Frandsen, M. W. Meisel, M. V. Manuel, R. Dingreville, and J. J. Hamlin, Phys. Rev. B **106**, 014418 (2022).

[25] K. Jin, B. C. Sales, G. M. Stocks, G. D. Samolyuk, M. Daene, W. J. Weber, Y. Zhang, and H. Bei, Sci. Rep. **6**, 20159 (2016).

[26] O. Schneeweiss, M. Friák, M. Dudová, D. Holec, M. Šob, D. Kriegner, V. Holé, P. Beran, E. P. George, J. Neugebauer, and A. Dlouhý, Phys. Rev. B **96**, 014437 (2017).

[27] J. Kamarád, M. Friák, J. Kaštil, O. Schneeweiss, M. Šob, and A. Dlouhý, J. Magn. Magn. Mater. **487**, 165333 (2019).

[28] B. Schuh, F. Mendez-Martin, B. Völker, E. George, H. Clemens, R. Pippan, and A. Hohenwarter, Acta Mater. **96**, 258 (2015).

[29] F. Otto, A. Dlouhý, K. G. Pradeep, M. Kuběnová, D. Raabe, G. Eggeler, and E. P. George, Acta Mater. **112**, 40 (2016).

[30] Y. J. Li, A. Savan, A. Kostka, H. S. Stein, and A. Ludwig, Mater. Horiz. **5**, 86 (2018).

[31] Y. Miyajima, T. Nagata, K. Takeda, S. Yoshida, S. Yasuno, C. Watanabe, I. Kazuhiro, H. Adachi, and N. Tsuji, Sci. Rep. **12**, 16776 (2022).

[32] X. Wang, R. R. De Vecchis, C. Li, H. Zhang, X. Hu, S. Sridar, Y. Wang, W. Chen, and W. Xiong, Sci. Adv. **8**, eabo7333 (2022).

[33] S.-M. Na, P. K. Lambert, and N. J. Jones, AIP Adv. **11**, 015210 (2021).

[34] C.-H. Lee, H.-H. Chin, K.-Y. Zeng, Y.-J. Chang, A.-C. Yeh, J.-W. Yeh, S.-J. Lin, C.-C. Wang, U. Glatzel, and E.-W. Huang, Front. Mater. **9** (2022).

[35] Y.-Y. Tan, Z.-J. Chen, M.-Y. Su, G. Ding, M.-Q. Jiang, Z.-C. Xie, Y. Gong, T. Wu, Z.-H. Wu, H.-Y. Wang, and L.-H. Dai, J. Mater. Sci. Technol. **104**, 236 (2022).

[36] C. Wagner, A. Ferrari, J. Schreuer, J.-P. Couzinié, Y. Ikeda, F. Körmann, G. Eggeler, E. P. George, and G. Laplanche, Acta Mater. **227**, 117693 (2022).

[37] C. D. Woodgate and J. B. Staunton, Phys. Rev. B **105**, 115124 (2022).

[38] F. Moitzi, L. Romaner, A. V. Ruban, and O. E. Peil, Accurate *ab initio* modeling of solid solution strengthening in high entropy alloys, arXiv:2209.12462.

[39] A. D. Hillier, S. J. Blundell, I. McKenzie, I. Umegaki, L. Shu, J. A. Wright, T. Prokscha, F. Bert, K. Shimomura, A. Berlie, H. Alberto, and I. Watanabe, Nat. Rev. Methods Primers **2**, 4 (2022).

[40] K. A. Petersen, J. Black, and B. A. Frandsen, BEAMS: Basic and effective analysis for muon spin spectroscopy (2021), https://github.com/FrandsenGroup/beams.

[41] See Supplemental Material at http://link.aps.org/supplemental/10.1103/PhysRevB.108.094437 for additional details of sample characterization and data analysis.

[42] F. Otto, N. Hanold, and E. George, Intermetallics **54**, 39 (2014).

[43] E. J. Pickering, R. Muñoz-Moreno, H. J. Stone, and N. G. Jones, Scr. Mater. **113**, 106 (2016).

[44] G. Kresse and J. Hafner, Phys. Rev. B **47**, 558 (1993).

[45] G. Kresse and J. Hafner, Phys. Rev. B **49**, 14251 (1994).

[46] G. Kresse, J. Non-Cryst. Solids **192-193**, 222 (1995).

[47] P. E. Blöchl, Phys. Rev. B **50**, 17953 (1994).

[48] G. Kresse and D. Joubert, Phys. Rev. B **59**, 1758 (1999).

[49] J. P. Perdew, K. Burke, and M. Ernzerhof, Phys. Rev. Lett. **77**, 3865 (1996).

[50] S. Blundell, *Magnetism in Condensed Matter* (Oxford University Press, Oxford, New York, 2001).

[51] Y. Uemura, in *Muon Science: Muons in Physics, Chemistry and Materials*, edited by S. Lee, R. Cywinski, and S. Kilcoyne (Taylor & Francis, New York, 1999).

[52] L. N. Mulay and E. A. Boudreaux, *Theory and Applications of Molecular Diamagnetism* (Wiley, New York, 1976).

[53] G. Cao, J. E. Crow, R. P. Guertin, P. F. Henning, C. C. Homes, M. Strongin, D. N. Basov, and E. Lochner, Solid State Commun. **113**, 657 (2000).

[54] H. Kaldarar, E. Royanian, H. Michor, G. Hilscher, E. Bauer, A. Gribanov, D. Shtepa, P. Rogl, A. Grytsiv, Y. Seropegin, and S. Nesterenko, Phys. Rev. B **79**, 205104 (2009).

[55] T. Groń, A. W. Pacyna, and E. Malicka, Solid State Phenomena **170**, 213 (2011).

[56] M. M. Markina, B. V. Mill, E. A. Zvereva, A. V. Ushakov, S. V. Streltsov, and A. N. Vasiliev, Phys. Rev. B **89**, 104409 (2014).

[57] M. McElfresh, *Fundamentals of Magnetism and Magnetic Measurements* (Quantum Design, San Diego, California, 1994), https://qdusa.com/siteDocs/appNotes/FundPrimer.pdf.

[58] D. Ma, B. Grabowski, F. Körmann, J. Neugebauer, and D. Raabe, Acta Mater. **100**, 90 (2015).

[59] D. Billington, A. D. N. James, E. I. Harris-Lee, D. A. Lagos, D. O'Neill, N. Tsuda, K. Toyoki, Y. Kotani, T. Nakamura, H. Bei, S. Mu, G. D. Samolyuk, G. M. Stocks, J. A. Duffy, J. W. Taylor, S. R. Giblin, and S. B. Dugdale, Phys. Rev. B **102**, 174405 (2020).

[60] P. Rhodes, E. P. Wohlfarth, and H. Jones, Proc. R. Soc. London A **273**, 247 (1963).